Acta Oceanol. Sin., 2023, Vol. 42, No. 10, P. 84–96
https://doi.org/10.1007/s13131-023-2215-5
http://www.aosocean.com
E-mail: ocean2@hyxb.org.cn

First assessment of Noise-Equivalent Sigma-Zero in GF3-02 TOPSAR mode with sea surface wind speed retrieval

Junxin Yang[1, 2, 3], Lihua Zhong[1, 2*], Xinzhe Yuan[4], Xiaochen Wang[1, 2], Bing Han[1, 2], Yuxin Hu[1, 2, 3]

[1] Aerospace Information Research Institute, Chinese Academy of Sciences, Beijing 100094, China

[2] Key Laboratory of Technology in Geo-Spatial Information Processing and Application Systems, Chinese Academy of Sciences, Beijing 100190, China

[3] School of Electronic, Electrical and Communication Engineering, University of Chinese Academy of Sciences, Beijing 100049, China

[4] National Satellite Ocean Application Service, Beijing 100081, China

Received 6 November 2022; accepted 22 May 2023

Abstract

Gaofen-3-02 (GF3-02) is the first C-band synthetic aperture radar (SAR) satellite with terrain observation with progressive scans of SAR (TOPSAR) imaging mode in China, which plays an essential role in marine environment monitoring. Given the weak scattering characteristics of the ocean, the system thermal noise superimposed on SAR images has significant interference, especially in cross-polarization channels. Noise-Equivalent Sigma-Zero (NESZ) is a measure of the sensitivity of the radar to areas of low backscatter. The NESZ is defined to be the scattering cross-section coefficient of an area which contributes a mean level in the image equal to the signal-independent additive noise level. For TOPSAR, NESZ exhibits the shape of the SAR scanning gain curve in the azimuth and the shape of the antenna pattern in the range. Therefore, the accurate measurement of NESZ plays a vital role in the application of spaceborne SAR sea surface cross-polarization data. This paper proposes a theoretical calculation method for the NESZ curve in GF3-02 TOPSAR mode based on SAR noise inner calibration data and the imaging algorithm. A method for correcting the error existing in the theoretical curve of NESZ is also proposed according to the relationship between sea surface backscattering and wind speed and the same characteristics of target scattering in the overlapping area of adjacent sub-swaths. According to assessment with wide-swath TOPSAR cross-polarization data, the GF3-02 TOPSAR mode has a very low thermal noise level, which is better than –33 dB at the edge of each beam, and controlled below –38 dB at the center of the beam. The two-dimensional reference curves of the NESZ of each beam are provided to the GF3-02 TOPSAR users. After discussing the relationship between normalized radar cross section (NRCS) and wind speed, we provide a formula for NRCS related to wind speed and radar incidence angle. Compared with the NRCS derived from this formula and the NESZ-subtracted NRCS of SAR images, the bias is –0.004 8 dB, the Root Mean Square Error is 1.671 dB and the correlation coefficient is 0.939.

Key words: GF3-02, TOPSAR, Noise-Equivalent Sigma-Zero (NESZ), cross-polarization, normalized radar cross section (NRCS), sea surface wind

Citation: Yang Junxin, Zhong Lihua, Yuan Xinzhe, Wang Xiaochen, Han Bing, Hu Yuxin. 2023. First assessment of Noise-Equivalent Sigma-Zero in GF3-02 TOPSAR mode with sea surface wind speed retrieval. Acta Oceanologica Sinica, 42(10): 84–96, doi: 10.1007/s13131-023-2215-5

1 Introduction

Synthetic Aperture Radar (SAR) is an important microwave remote sensing method with all-day and all-weather working capabilities. With the increasing quantitative application of SAR, users rely more on SAR radiation accuracy. In other words, whether SAR images can reflect the absolute normalized radar cross section (NRCS) of natural objects plays a crucial role in the application of SAR quantification. However, there is noise interference in the entire signal processing process of the SAR system, so the SAR-derived NRCS cannot accurately reflect the scattering characteristics of actual ground objects. SAR images are not only affected by speckle noise which can be eliminated by multi-look processing, but also by thermal noise caused by temperature-induced microscopic motion into the SAR receiver, and is digitally amplified by the radar's inner circuitry and signal. In the imaging process, the radiation correction that adapts to the characteristics of the useful signal but not the characteristics of the noise affects the spatial distribution of the noise power.

Thermal noise is often neglected in many applications because, in most cases, the signal power is sufficient to mask the thermal noise variation. Usually, thermal noise is hardly noticeable in SAR co-polarization (HH/VV) channel data. However, thermal noise is a major obstacle in analyzing cross-polarization (HV/VH) channel images with low backscatter, such as calm seas and lakes. As a result, when the signal-to-noise ratio (SNR) is low, the NRCS value of the target calculated directly on the SAR image is inaccurate (Shi et al., 2021). For example, in the field of ocean remote sensing, the SAR-derived NRCS on the sea surface is mainly caused by Bragg scattering (Valenzuela, 1978), which is caused by the resonance interaction between the magnetic wave

Foundation item: The National Natural Science Foundation of China under contract No. 41976169.
*Corresponding author, E-mail: zhonglh@aircas.ac.cn

emitted by the radar and the centimeter-scale short wave, and is mainly related to the radar parameters and the characteristics of the sea surface. Due to the weak backscattering of the sea surface, the influence of thermal noise in the SAR system can not be ignored especially for the application of cross-polarization wind speed retrieval. Similarly, the presence of system noise affects the accuracy of applications in water body polarization calibration (Lu and Yang, 2013), sea ice monitoring (Scheuchl and Cumming, 2005), sea surface oil spills (Angelliaume et al., 2018), soil moisture monitoring, etc. Therefore, for spaceborne SAR systems (e.g., Sentinel-1 or RADARSAT-2), the NESZ values in the range direction are recorded in the metadata.

On November 23, 2021, China successfully launched the 1-m resolution C-band SAR satellite, also known as the Gaofen-3-02 (GF3-02) satellite, at the Jiuquan Satellite Launch Center. The satellite further enhances the operational observation capabilities of China's marine remote sensing. It can meet the application which needs of marine rights and maintenance, marine disaster prevention which and mitigation and dynamic marine environment monitoring. The primary payload is C-band SAR with a maximum resolution of 1 m. Like GF3 (Han et al., 2018), it also has 12 imaging modes, except that the Terrain observation with progressive scans of SAR (TOPSAR) mode is used instead of the ScanSAR mode used by GF3. Both TOPSAR mode and ScanSAR mode with the same wide-swath imaging ability utilize the data acquisition method of multiple sub-swaths, but TOPSAR avoids the scallop effect in ScanSAR mode images. However, due to the inconsistency of thermal noise in each sub-swath system and the compensation and correction of azimuth scanning gain, the backscattering coefficient of the image is discontinuous between sub-swaths along the range, and there is light and dark alternation in the range. Therefore, it is necessary to accurately assess the thermal noise power in GF3-02 TOPSAR images for more precise application.

Noise-Equivalent Sigma-Zero (NESZ) measures a system's sensitivity to regions of low radar backscatter, which is the contribution of instrument thermal noise observed in the images (Freeman, 1992). It is given by the value of the backscattering coefficient corresponding to a SNR equal to 1. It includes all errors caused by the system, such as instrument thermal noise, link gain, antenna patterns, and processing filters (Martone et al., 2013). The accurate measurement of the NESZ plays an important role in the application of spaceborne SAR cross-polarization data. At present, the estimation scheme of NESZ mainly has the following methods. (1) Measurement of on a scene is with ideal zero backscatter, such as calm water or a flat surface. It is also the usual method for NESZ analysis of many SAR satellites (Albright and Nicoll, 2002; Torres et al., 2017; Martone et al., 2013). However, this method requires very high-quality irradiated area. (2) Based on the reciprocity property, the minimum eigenvalue estimator (MEE) (Hajnsek et al., 2003) and maximum likelihood estimation (MLE) (Moon et al., 2010) techniques can be used to derive NESZ from cross-polarization images. Furthermore, Shi (Shi et al., 2021) proposed the minimum noise envelope estimator (MNEE) to derive the NESZ of the GF3 image in Quad-polarization Strip Ⅰ (QPS Ⅰ) and Quad-polarization Strip Ⅱ (QPS Ⅱ) modes by using the sea surface as a reference. However, this method must ensure the use of a reflection-symmetric target, that is, the HV and VH reflection characteristics of the target should be the same, and this method can only obtain the NESZ of the cross-polarization channel of the SAR full-polarization mode. (3) Based on hardware measurement, a noise calibration loop is currently utilized for the SAR payload, which only receives the system thermal noise as an echo signal, and then passes through the same ground imaging processing system as the SAR signal and finally outputs the NESZ in the SAR image. This method can accurately obtain the noise power of the receiver, and then combined with the modulation gain of the SAR imaging processing algorithm to the system noise, the NESZ in the SAR image can be accurately obtained. However, in the implementation process, the same imaging processing flow as the SAR signal needs to be used for the noise calibration signal, which requires a large amount of calculation and a high time cost.

Because of the above-mentioned NESZ acquisition methods and existing problems, this paper derives a theoretical calculation method for the NESZ curve of GF3-02 TOPSAR mode, and proposes an error correction method for the NESZ theoretical curve of sea surface images under low sea conditions. The specific process includes: calculating the noise power of the inner calibration data, calculating the noise gain in the SAR imaging process, combining the noise gain and the inner calibration noise power to obtain the calculated NESZ, and correcting the error of the calculated NESZ value to obtain the estimated NESZ of the SAR image. The remainder of the paper starts with Section 2, which mainly introduces the GF3-02 TOPSAR imaging mode and the data used in this paper and then presents the NESZ estimation method. Next, Section 3 introduces the NESZ estimation results combined with the real GF3-02 TOPSAR images. Section 4 summarizes the results of experiments with some discussion, and Section 5 gives the conclusions of this paper.

2 Materials and methods

2.1 *Data*

2.1.1 *GF3-02 TOPSAR data*

The TOPSAR mode is an important method for SAR in large-swath observation (Yin et al., 2021). During TOPSAR imaging, the antenna beam scans in two dimensions in the range and azimuth to realize large-swath imaging and avoid the azimuth scallop phenomenon, as shown in Fig. 1. The working modes of TOPSAR commonly used by GF3-02 for ocean monitoring include: wide-swath TOPSAR (5 sub-swaths) and narrow-swath TOPSAR (3 sub-swaths). The resolution, imaging width and polarization requirements of the three imaging modes are shown in Table 1. The GF3-02 TOPSAR products used in this paper are all produced by the National Satellite Ocean Application Service (NSOAS).

We collected the GF3-02 wide-swath TOPSAR images pro-

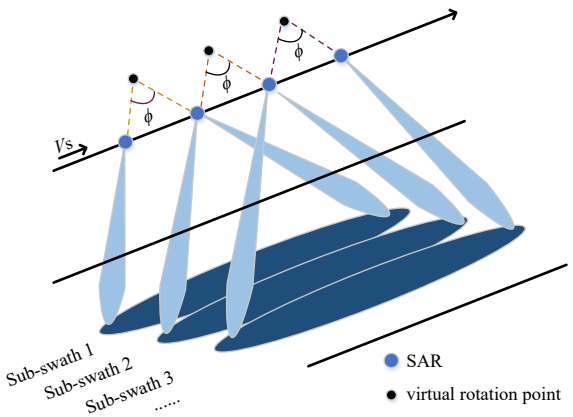

Fig. 1. Schematic diagram of TOPSAR imaging mode.

Table 1. The working mode and capability of GF3-02 TOPSAR mode

Working mode	Resolution/m	Width/km	Polarization
Narrow-swath TOPSAR	50	300	HH+HV/VH+VV
Wide-swath TOPSAR	100	500	HH+HV/VH+VV

duced by NSOAS as of August 2022 to assess the NESZ. Since GF3-02 SAR is still in the orbit testing stage, we only selected six sea surface images with clean scenes, no terrain or other interference factors and low winds ($U_{10} < 13.8$ m/s), as shown in Table 2 (Fan et al., 2020). These data cover all beams of wide-swath TOPSAR, and the polarization modes are VH and VV. Unfortunately, only one image for beam selection of S2, S3, S4, S5 and S6 meets the NESZ assessment criteria. Figure 2 shows an VH polarization image of the waters near the West Coast of the United States obtained by GF3-02 TOPSAR imaging mode on April 24, 2022, with orbit ID 2204 and scene ID 29880. And the red curve represents the NESZ curve of each subswath. The NESZ curves between each sub-swath are different and discontinuous, which changes with the range antenna pattern. There is a bright step phenomenon in the region where the sub-swaths are connected. The thermal noise of the whole image also changes in the azimuth, and there is a residual scallop phenomenon. Specifically, the areas near the edge of the beam are brighter than the areas in the center of the beam because they have higher noise power, especially in the range of the sub-swath to the edge area.

Table 2. The selected GF3-02 SAR products

Orbit ID	Scene ID	Location	Imaging time	Beam code
1736	17852	21.5°N, 127.2°E	March 23, 2022	S1–S5
1959	22847	34.1°N, 137.2°E	April 7, 2022	S1–S5
1980	23839	40.4°N, 135.1°E	April 9, 2022	S2–S6
2135	27832	31.9°N, 120.3°E	April 20, 2022	S1–S5
2204	29879	43.5°N, 134.4°E	April 24, 2022	S1–S5
2204	29880	39.4°N, 135.2°E	April 24, 2022	S1–S5
2204	29881	34.0°N, 136.3°E	April 24, 2022	S1–S5

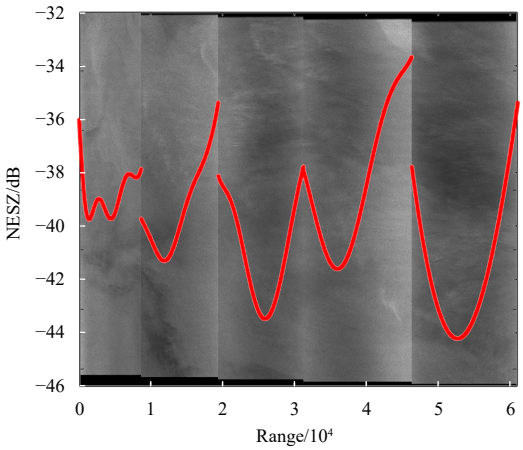

Fig. 2. A VH polarization image of the seas near the west coast of the United States obtained by GF3-02 wide-swath TOPSAR imaging mode on April 24, 2022, with orbit ID 2204 and scene ID 29880, where the red curve represents the NESZ curve of each subswath.

2.1.2 *ERA-5 data*

ERA-5 is the fifth generation of the European Centre for Medium-Range Weather Forecasts (ECMWF) global climate reanalysis data, which provides wind field data with a temporal resolution of 1 h and a spatial resolution of 0.25° latitude and longitude. We chose ERA-5 wind data that matches SAR data spatially and temporally (the time interval is within 30 min) as the reference wind field for co-polarization wind speed retrieval and cross-polarization wind speed model fitting.

2.2 *NESZ estimation method*

The GF3-02 SAR raw data includes head and tail noise calibration data and imaging data. The estimation method of NESZ (P_N) of the GF3-02 SAR image proposed in this paper is shown in Eq. (1), and the flow chart of the method is shown in Fig. 3. Firstly, the noise power P_{N_wn} is calculated according to the inner calibration data of the SAR raw data. In the absence of ground interference signals in the same frequency band, the signal source of the head and tail noise calibration data is mainly system thermal noise. By using statistical analysis methods, the energy and distribution characteristics of noise signals can be calculated, thereby calculating the noise level of the system; Secondly, the gain G of the imaging process on the noise signal is calculated by combining SAR imaging data and SAR imaging algorithms; then the initial value of NESZ is obtained by combining P_{N_wn} and G; finally, the noise calibration power may be inconsistent with the absolute value of the noise power superimposed on the SAR signal, resulting in a certain absolute error between the initial NESZ value of the SAR image calculated using the above method and the actual value, which finally needs to be corrected by the correction factor K.

$$P_N = P_{N\_wn} \cdot G \cdot K. \tag{1}$$

2.2.1 *Noise power of inner calibration data*

GF3 series satellites has a noise inner calibration mode (Zhang, 2017). According to the instruction manual of the GF3-02 system, the noise power is obtained by counting the variance of the noise calibration data in the SAR raw data. In addition, it should be noted that the manual gain control (MGC) used for

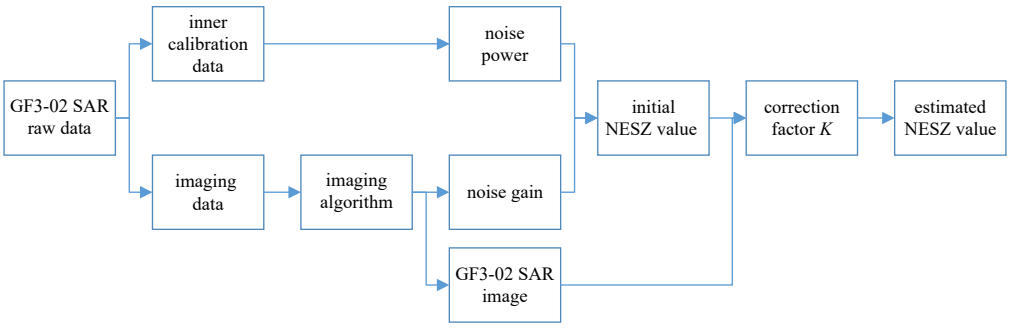

Fig. 3. Flow chart of NESZ estimation method for GF3-02 TOPSAR imaging mode.

noise calibration differs from that used for the imaging process, and the difference in MGC should also be considered in calculating the noise power. MGC is a method of manually adjusting, remotely controlling, and program-controlled receiver gain to determine signal strength. The purpose is to match the system gain and dynamic range with the received signal strength and dynamic range, achieving optimal signal reception to avoiding saturation or clipping of the signal. The noise power of noise calibration data is set as P_{N_in}, MGC used for noise calibration is MGC_1, MGC used at imaging time is MGC_2, and the noise power relative to the SAR echo signal during imaging is P_{N_wn}, which can be expressed as:

$$P_{N\_\text{wn}} = P_{N\_\text{in}} \cdot \text{MGC}_1/\text{MGC}_2. \tag{2}$$

2.2.2 *Noise gain of TOPSAR imaging algorithm*

In the process of SAR imaging processing and radiation correction, not only is the SAR echo signal corrected but also the thermal noise signal. Therefore, the noise gain can be calculated according to the radiation correction processing of the SAR data processing system. Combining GF3-02 SAR imaging processing and the radiation correction process, this paper provides a theoretical calculation method of noise gain in SAR imaging processing. Figure 4 shows the propagation process of the SAR signal. The radar signal is first transmitted by the radar transmitter, modulated by the transmitting antenna and attenuated by the spherical wave with radius R to the target. The target scattering echo is also attenuated by the spherical wave with a radius R, received by the receiving antenna and transmitted to the radar receiver. According to the analysis of the SAR radar equation in Freeman and Curlander (1989), after digitization but before any signal processing (such as azimuth or range compression), the expected power in a single pulse of backscattering coefficient received from distributed target is as follows (Zhong et al., 2019):

$$P_\text{r} = \frac{P_\text{t} G^2(\theta,\phi) K_\text{r} \lambda^2 \sigma^0 A_\text{t}}{(4\pi)^3 R^4(\theta) L} + P_\text{n}, \tag{3}$$

where P_r is the total backscatter power obtained by the receiving antenna, P_t is the total transmitter power, $G^2(\theta,\phi)$ is the gain of the antenna at local incidence angle θ and azimuth angle ϕ, λ is the electromagnetic wave wavelength, K_r is the receiver gain including fixed gain and MGC, $R(\theta)$ is the slant range at local incidence angle θ, σ^0 is the uniform normalized cross section, A_t is the area of resolution cell, L is the system loss and P_n is the additive noise. Finally, the radar echo is imaged by the SAR imaging algorithm. Therefore, the radiation correction processing of the SAR ground processing system mainly considers aspects such as the antenna and propagation process, SAR receiver gain and imaging processor (Curlander and McDonough, 1991).

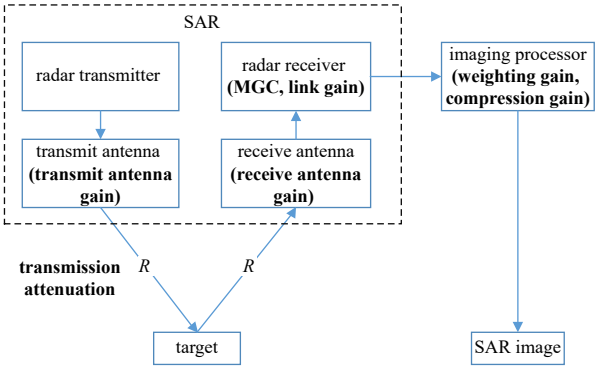

Fig. 4. Schematic diagram of synthetic aperture radar signal propagation, where bold font represents the signal gain during SAR signal propagation and processing.

This section introduces the theoretical calculation of noise gain in combination with the radiation correction process of the GF3-02 TOPSAR imaging algorithm. In the radiation correction process, correction processing of transmission attenuation G_ta, receiver link gain G_lg, receiver gain control G_MGC, and imaging processor gain need to be performed.

During TOPSAR imaging, the azimuth beam is rapidly scanned from the back to the front to achieve short-term coverage of large scenes in the azimuth direction. Each scattering point basically undergoes a complete antenna pattern. Therefore, compared with ScanSAR, the phenomenon of inconsistent azimuthal radiation of scattering points is significantly reduced, and the scallop effect is effectively eliminated. The GF3-02 TOPSAR imaging mode utilizes an imaging algorithm based on azimuth preprocessing and Extended Chirp Scaling (ECS), as shown in Fig. 5. Since the TOPSAR azimuth beam scan angle is much larger than the beam width, the azimuth pulse repetition frequency (PRF) is much smaller than the actual azimuth Doppler bandwidth. A simple processing method is to use the azimuth pre-filtering method to first upsample the azimuth direction. After upsampling, the PRF is larger than the Doppler bandwidth, and then the ECS algorithm of ScanSAR imaging is used for processing. In the ECS algorithm, range compression gain G_crg, range weighting gain G_wrg (bandwidth truncation), azimuth compression gain G_caz, azimuth weighting gain G_waz, azimuth antenna pattern gain G_paz, and range antenna pattern gain G_prg all produce additional gains on SAR echo signals and noise. It should be noted that in the SAR data radiometric correction, the gain of the algorithm to the system thermal noise in the weighted gain is different from the SAR echo signal; that is, the weighted function is different from the echo signal and noise gain.

(1) For range weighting gain G_wrg, the spectrum of the SAR range echo signal is approximately rectangular, and the spectrum of the matched filter is also rectangular, so the gain of the range weighting function can be calculated directly. For the echo signal, the range weighting function gain G_wrg can be expressed as:

$$G_\text{wrg} = \sqrt{\frac{\sum_{i=-\frac{N_\text{wr}}{2}}^{\frac{N_\text{wr}}{2}} \left(WIN_\text{rg}(i)\right)^2}{N_\text{wr}}}, \tag{4}$$

where WIN_rg is the range weighting function, and N_wr is the range weighting length, as shown in Fig. 6. SAR echo and noise also lose spectral energy beyond the weighting function (processing bandwidth), but echo signal loss has been considered in the process of range compression gain compensation. Because the range compression gain is for the SAR echo signal, it does not generate gain for noise power. The energy loss outside the weighting function needs to be considered for noise. Therefore, noise range weighting gain GN_wrg can be expressed as

$$GN_\text{wrg} = G_\text{wrg} \cdot \sqrt{\frac{N_\text{wr}}{N_\text{r}}} = \sqrt{\frac{\sum_{i=-\frac{N_\text{wr}}{2}}^{\frac{N_\text{wr}}{2}} \left(WIN_\text{rg}(i)\right)^2}{N_\text{r}}}, \tag{5}$$

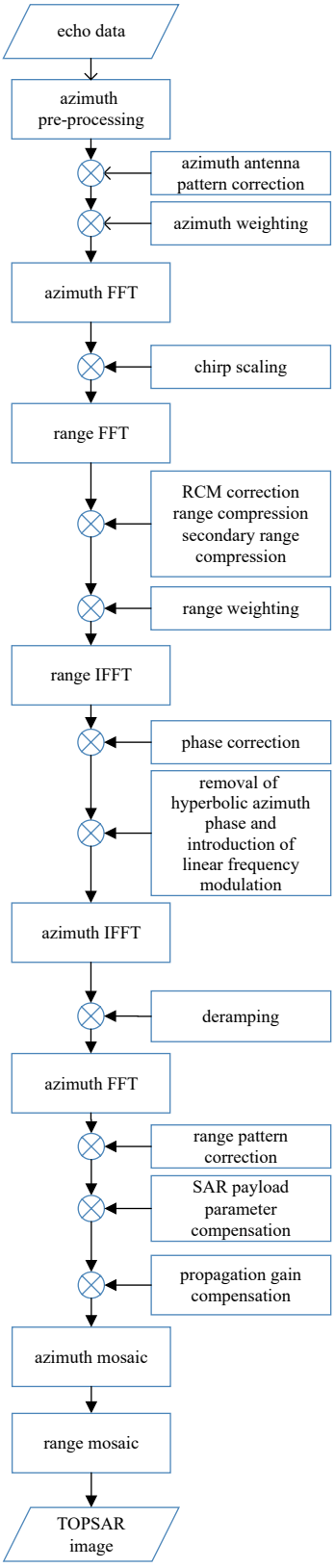

Fig. 5. Flow chart of TOPSAR imaging algorithm.

where N_r is the length of the image in the range. Therefore, the noise gain calculation needs to subtract the SAR echo signal range weighting gain G_{wrg} and add the noise range weighting gain GN_{wrg}.

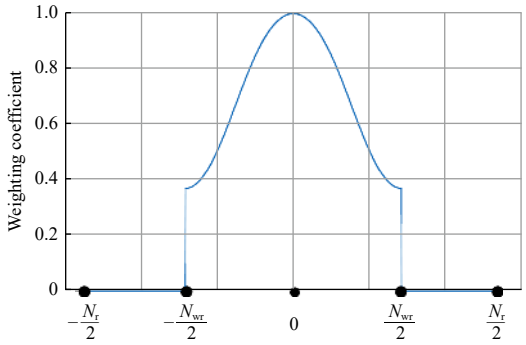

Fig. 6. TOPSAR weighting function in range.

(2) For azimuth weighting gain G_{waz} of the SAR echo signal, the gain of the azimuth weighting function is similar to that calculated in Eq. (4):

$$G_{\mathrm{waz}} = \sqrt{\frac{\sum_{i=-\frac{N_{\mathrm{wa}}}{2}}^{\frac{N_{\mathrm{wa}}}{2}} \left(WIN_{\mathrm{az}}(i)\right)^2}{N_{\mathrm{wa}}}}, \tag{6}$$

where WIN_{az} is the azimuth weighting function, and N_{wa} is the azimuth weighting length. However, for the noise, the spectrum shape is no longer rectangular after the modulation and compensation of the azimuth antenna pattern, so the influence of the antenna pattern should be considered in the calculation of the gain of the azimuth weighting function. The antenna pattern correction coefficient should also be regarded as a weighting function, and the two can be combined, as calculated by Eq. (5). The noise azimuth weighting gain can be expressed as:

$$\begin{aligned} GN_{\mathrm{waz}} &= \sqrt{\frac{\sum_{i=-\frac{N_{\mathrm{wa}}}{2}}^{\frac{N_{\mathrm{wa}}}{2}} \left(WIN_{\mathrm{az}}(i) \cdot G_{\mathrm{paz}}(i)\right)^2}{N_{\mathrm{wa}}}} \cdot \sqrt{\frac{N_{\mathrm{wa}}}{N_{\mathrm{a}}}} \\ &= \sqrt{\frac{\sum_{i=-\frac{N_{\mathrm{wr}}}{2}}^{\frac{N_{\mathrm{wr}}}{2}} \left(WIN_{\mathrm{rg}}(i) \cdot G_{\mathrm{paz}}(i)\right)^2}{N_{\mathrm{a}}}}, \end{aligned} \tag{7}$$

where N_{a} is the length of the image in the azimuth. Similarly, the noise gain calculation needs to subtract the SAR echo signal azimuth weighting gain G_{waz} and add the noise azimuth weighting gain GN_{waz}. In addition, multi-look processing is generally used to reduce speckle noise. The specific operation is to reduce the processor's bandwidth in the azimuth and range, divide the spectrum into several imaging segments, and perform incoherent superposition. Therefore, due to multi-look processing, the calculation of the noise gain by the weighting function also changes for the system noise signal. On the one hand, multi-look processing will not cause additional gain for the range function gain in the range. On the other hand, because the noise gain is modulated by the azimuth antenna pattern in the azimuth direction, the azimuth spectrum of each segment is not consistent after azimuth multi-look processing. Therefore, the noise azimuth weighted gain needs to be superimposed and averaged, which can be expressed as:

$$GN_{\mathrm{waz}}=\sqrt{\frac{\sum_{n=1}^{N}\sum_{i=-\frac{N_{\mathrm{wr}}}{2}}^{\frac{N_{\mathrm{wr}}}{2}}\left(WIN_{\mathrm{rg}}(i)\cdot G_{\mathrm{paz}}(i)\right)^{2}}{N_{\mathrm{a}}}}. \tag{8}$$

Then, the TOPSAR imaging algorithm needs azimuth prefiltering before the CS algorithm to eliminate spectrum aliasing. After the CS algorithm, the azimuth SPECAN algorithm is introduced to adjust azimuth pixel spacing. The azimuth prefilter performs upsampling on the SAR echo signal and noise, and the energy of the echo signal and noise is also reduced by M times, so the azimuth prefilter gain is $G_{\mathrm{azpre}}=M$. The azimuth SPECAN algorithm itself does not generate processing gain, but after the azimuth SPECAN processing, unlike the strip mode, the TOPSAR mode image appears in the Doppler frequency domain. At this time, due to its physical characteristics, the SAR echo signal is distributed in the spectrum range determined by the antenna scanning angle. In contrast, the noise is distributed in the whole spectrum. Therefore, the azimuth SPECAN algorithm brings additional processing gain to the noise GN_{specan}, which can be expressed as:

$$GN_{\mathrm{specan}}=\sqrt{\mathrm{PRF}/\left(\left(N_{\mathrm{pulse}}/\mathrm{PRF}\right)\cdot K_{\mathrm{rot}}+\mathrm{PRF}\right)}, \tag{9}$$

where N_{pulse} is the number of azimuth pulses and K_{rot} is the change rate of Doppler the center of the TOPSAR target echo with azimuth time. Considering the diffusion of target energy, the gain of azimuth SPECAN operation on SAR signal is $G_{\mathrm{specan}}=\sqrt{N_{\mathrm{pulse}}}$.

Finally, the azimuth noise of strip mode is constant, but the antenna gain of TOPSAR is different at different scanning angles due to azimuth beam scanning, so the azimuth scanning gain needs to be compensated in the process of imaging processing and radiometric correction. This process also modulates the thermal noise, which causes the noise to change along the azimuth on the image, and the trend is consistent with the antenna azimuth scanning gain curve. The GF3-02 TOPSAR image is obtained in the Doppler frequency domain, and the azimuth position of the image is related to the Doppler center frequency within the target irradiation time. Therefore, the scanning angle corresponding to the target can be calculated by the Doppler frequency of the target:

$$\phi=\arcsin\left(\frac{\left(F_{\mathrm{a}}-f_{\mathrm{dc}}\right)\cdot\lambda}{2V}\right), \tag{10}$$

where F_{a} is azimuth Doppler frequency, f_{dc} is Doppler centroid frequency when the azimuth scanning angle is zero, λ is the radar wavelength and V is the satellite velocity. f_{dc} can be ignored due to the existence of two-dimensional attitude guidance. Then, the azimuth scanning gain G_{az} of the scanning angle ϕ can be obtained by interpolating on the scanning gain curve.

$$G_{\mathrm{az}}(\phi)=\frac{1}{g(\phi)}, \tag{11}$$

where $g(\phi)$ is the scanning gain curve of GF3-02 TOPSAR imaging mode.

To sum up, details of SAR echo and noise gain calculation during imaging processing are shown in Table 3. The two-dimensional gain $G(\phi,\theta)$ generated by the GF3-02 TOPSAR imaging algorithm on noise can be expressed as:

$$G(\phi,\theta)=\frac{G_{\mathrm{MGC}}\cdot G_{\mathrm{ta}}(\theta)\cdot G_{\mathrm{lg}}\cdot G_{\mathrm{prg}}(\theta)\cdot GN_{\mathrm{wrg}}\cdot GN_{\mathrm{waz}}\cdot G_{\mathrm{azpre}}\cdot GN_{\mathrm{specan}}\cdot G_{az}(\phi)}{G_{\mathrm{crg}}(\theta)\cdot G_{\mathrm{caz}}\cdot G_{\mathrm{wrg}}\cdot G_{\mathrm{waz}}\cdot G_{\mathrm{specan}}}. \tag{12}$$

2.2.3 *Correction factor K*

There may be some errors between the inner calibration noise power and the noise power actually superimposed on the SAR echo signal, especially in the TOPSAR imaging mode. The noise power between different sub-swaths is inconsistent. Moreover, the inner calibration data of GF3-02 SAR noise only represents the system noise of the first sub-swath, and the noise powers of other sub-swaths are unknown, so the correction factor K is needed to compensate for the errors of the initial value of NESZ. To solve this problem, Park et al. proposed a two-step correction method by analyzing the thermal noise of the Sentinel-1 TOPSAR system (Park et al., 2018, 2019; Korosov et al., 2022). Firstly, it is considered that the NRCS after subtracting noise of each sub-swath of TOPSAR data on a calm sea surface decreases linearly along the range. Then the NESZ given by the Sentinel-1 noise file is scaled to find the scaling factor K_{ns} that makes the NRCS after subtracting noise has the strongest linear correlation along the range. Finally, K_{pn} is calculated to correct the power discontinuity between sub-swaths. However, this method is only applicable to calm sea data. Under general sea conditions, the influence of sea surface wind speed cannot be ignored, because the contribution of wind speed to sea surface NRCS is much more significant than the contribution of incident angle. Therefore, this method is not suitable for a vast number of sea surface data. Given the shortcomings of the above methods, this paper proposes a corresponding solution, which combines the unique self-overlapping region of TOPSAR and the relationship between cross-polarization sea surface NRCS and sea surface wind speed.

Table 3. Details of SAR echo and noise gain calculation during imaging processing

Imaging process	SAR echo	System noise
MGC	G_{MGC}	G_{MGC}
Receiver link gain	G_{lg}	G_{lg}
Range compression gain	G_{crg}	G_{crg}
Azimuth compression gain	G_{caz}	G_{caz}
Azimuth antenna pattern correction	G_{paz}	GN_{waz}
Azimuth weighting gain	G_{waz}	GN_{waz}
Range weighting gain	G_{wrg}	GN_{wrg}
Range antenna pattern correction	G_{prg}	G_{prg}
Transmission attenuation	G_{ta}	G_{ta}
Azimuth prefilter gain	G_{azpre}	G_{azpre}
Azimuth SPECAN gain	–	G_{specan}
Azimuth scanning gain	G_{az}	G_{az}

Note: – represents no parameter.

First of all, the studies (Vachon and Wolfe, 2011; Zhang et al., 2012; van Zadelhoff et al., 2014; Ren et al., 2017; Wang et al., 2018) show that the NRCS of sea surface cross-polarization data is weakly dependent on the incident angle and relative wind direction, which is mainly dependent on the wind speed. In addition, as shown in Table 4, the beam width of GF3-02 in the range becomes smaller as the beam code increases. Thus, we ignored the dependence of NRCS on incident angle and relative wind direc-

Table 4. The look angle and range beam width of each beam code of the GF3-02 TOPSAR imaging mode

Beam code	S1	S2	S3	S4	S5	S6
Look angle/(°)	18.77	24.10	30.74	34.70	39.63	42.07
Beam width/(°)	10.24	8.83	6.45	6.15	4.27	4.04

tion in the highest sub-swath of the TOPSAR image in this paper. Therefore, the correction coefficient K of the highest sub-swath in the GF3-02 TOPSAR image can be obtained by calculating the linear correlation between the backscattering coefficient after subtracting the noise and the wind speed, which can be specifically expressed as

$$s(K) = 10\lg(\sigma^0_{SN} - K\cdot\sigma^0_N), \tag{13}$$

$$R(K) = \rho(s(K), U_{10}), \tag{14}$$

$$\max\{R(K)\} \Rightarrow K_{fit} = K, \tag{15}$$

where σ^0_{SN} is the NESZ-unsubtracted backscattering coefficient of the SAR image, σ^0_N is the initial value of NESZ, σ^0_{SN} is the backscattering coefficient after subtracting the noise with K as the scaling factor and U_{10} is the wind speed at 10 m above the sea surface, which can be retrieved from the sea surface data of the co-polarization channel obtained at the same time. In our previous research (Yang et al., 2022), we showed that CMOD5.N (Verhoef et al., 2008) and CMODH (Zhang et al., 2019) are the optimal empirical geophysical model functions (GMFs) for retrieving wind speed from GF3-02 SAR VV polarization or HH polarization, respectively. $R(K)$ is the Pearson correlation coefficient between $s(K)$ and U_{10}. Therefore, the flow chart of the NESZ correction factor of the highest sub-swath of GF3-02 TOPSAR image proposed in this paper is shown in Fig. 7.

There are overlapping regions between adjacent sub-swaths due to the unique characteristics of TOPSAR imaging. The different NRCS reflected by the overlapping regions between adjacent sub-swaths of the SAR image is caused by different noise levels. Taking a wide-swath TOPSAR mode with five sub-swaths as an example, the following relationship exists:

$$\begin{cases} \sigma_{i|i+1} + K_i\cdot P_{N\_wn}\cdot G_{i(i|i+1)} = A_{i(i|i+1)} \\ \sigma_{i|i+1} + K_{i+1}\cdot P_{N\_wn}\cdot G_{i+1(i|i+1)} = A_{i+1(i|i+1)} \end{cases}, i = 1,\ 2, 3,\ 4, \tag{16}$$

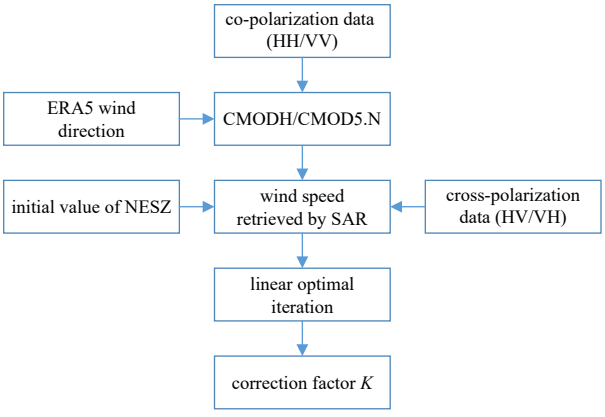

Fig. 7. Calculation flow of the correction factor K of the highest beam sub-swath of GF3-02 TOPSAR.

where $\sigma_{i|i+1}$ is the actual NRCS of the target in the overlapping area of sub-swath i and sub-swath $i+1$, K_i represents the noise correction factor of the sub-swath i, $G_{i(i|i+1)}$ and $G_{i+1(i|i+1)}$ represent the imaging noise gain of sub-swaths i and $i+1$ in the area where sub-swaths i and $i+1$ overlap, and $A_{i(i|i+1)}$ and $A_{i+1(i|i+1)}$ represent the NRCS retrieved from the SAR images of the area where sub-swaths i and $i+1$ overlap. Further, the following equation can be obtained:

$$A_{i(i|i+1)} - A_{i+1(i|i+1)} = K_i\cdot P_{N\_wn}\cdot G_{i(i|i+1)} - K_{i+1}\cdot P_{N\_wn}\times G_{i+1(i|i+1)}, i = 1, 2, 3, 4, \tag{17}$$

therefore, based on Eqs. (15) and (17), the correction factor K of all sub-swaths of GF3-02 TOPSAR data can be obtained, and then the denoising of cross-polarization data can be realized.

3 Results

In this section, we take the Fig. 2 as an example to show the effectiveness of the above method. In addition, Fig. 8 shows the image of Fig. 2 after subtracting the NESZ obtained by the estimation method proposed herein. In the process of noise subtraction, the backscattering coefficients of some pixels in the image inevitably have some negative values, especially in the subband edge areas, which are set to 0. Therefore, it may result in some spots near the boundary between sub-swaths in SAR images after noise subtraction. Comparing the VH polarization backscatter images before and after noise subtraction, it is obvious that the step phenomenon of the backscattering coefficient between image sub-swaths and the azimuthal residual scallop phenomenon caused by the discontinuity of thermal noise in each sub-swath has been effectively improved, especially the "white yarn" phenomenon shown in Fig. 2 has been removed. Therefore, the method proposed in this paper can effectively solve the problem that the image of GF3-02 TOPSAR is affected by thermal noise under low sea conditions. The specific NESZ estimation process of this GF3-02 TOPSAR image is as follows.

3.1 *Initial NESZ value*

As shown in Fig. 9, the blue curve represents the backscattering coefficient obtained when there is thermal noise in the VH polarization image, and the black curve represents the initial value of NESZ calculated from the internal calibration data of GF3-02 TOPSAR and the noise gain of the imaging algorithm. Obviously, the initial NESZ values of the GF3-02 TOPSAR image in

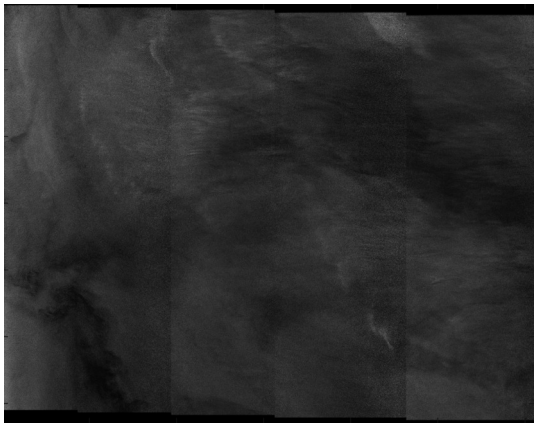

Fig. 8. The image after subtracting the noise obtained by the estimation method in this paper.

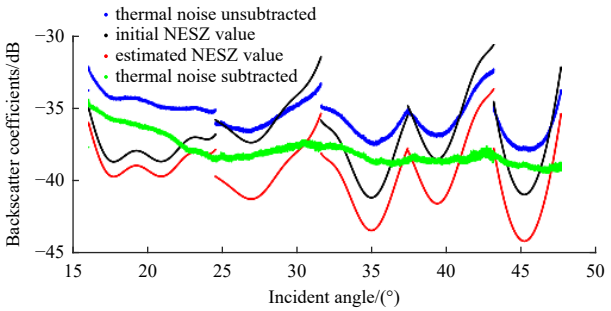

Fig. 9. The backscattering coefficient of VH polarization of this GF3-02 TOPSAR image before and after thermal noise subtraction and the NESZ before and after correction by correction factor K. The blue curve represents the NESZ-unsubtracted backscattering coefficients, the black line represents the initial value of NESZ, the red line represents the NESZ optimal estimation obtained by the method proposed in this paper, and the green represents the NESZ-subtracted backscattering coefficients.

the second sub-swath, the fourth sub-swath and the fifth sub-swath exceeded the backscattering coefficient derived from the SAR image. It is necessary to correct the error of the initial value of NESZ.

3.2 *Estimated NESZ value*

As shown in Fig. 7, the error correction of the initial value of NESZ in the highest sub-swath of this GF3-02 TOPSAR image was carried out. First, the VV polarization data of this TOPSAR image and the spatiotemporal matching ERA5 wind direction data were used as the input of the CMOD5.N model to retrieve the sea surface wind speed with high spatial resolution, which is about 1 km × 1 km in the range and azimuth. Figure 10 shows the backscattering coefficient of VV polarization and the sea surface wind retrieved from it. Then, the optimal correction factor was calculated according to Eqs (13), (14) and (15). Figure 11 shows the change of the correlation coefficient between the backscattering coefficient of VH polarization and wind speed after denoising with the correction factor K. The stronger the correlation, the more accurate the noise after correction by factor K. Obviously, the correlation coefficient increases first and then decreases with the increase in K. When $K = 0$, that is, when the noise is not subtracted, the correlation coefficient between the backscattering coefficient of VH polarization and wind speed is only 0.651. When K is 0.477, the linear correlation between the VH polarization backscattering coefficient after denoising and wind speed is the strongest (0.953). Therefore, it can be considered that the initial value correction factor K of NESZ in the fifth sub-swath is 0.477; that is, the inner calibration noise power has an error of −3.215 dB. Figure 12 shows the backscattering coefficient of VH polarization before and after NESZ subtraction and the change of NESZ before and after error correction with incident angle. The NESZ-subtracted backscattering coefficient of VH polarization does not show the shape of NESZ in the range, and the value of NESZ does not exceed the power of SAR echo signal superimposed with thermal noise. Figure 13 shows the scatter diagram of the change of VH polarization backscattering coefficient with wind speed, and more intuitively shows the relationship between VH polarization backscattering coefficient and wind speed before and after NESZ subtraction. Obviously, this method effectively solves the influence of the NESZ of the fifth sub-swath on the backscattering coefficients of the sea surface.

Finally, according to Eq. (17) and the correction factor of the fifth sub-swath, the correction factors K of the other four sub-swaths were obtained, as shown in Table 5. The correction factors of the five sub-swaths of this GF3-02 TOPSAR image are −1.032, −3.907, −2.266, −3.065 and −3.215 dB, respectively. This shows that the noise power of the calibration in the image is greater than the power superimposed on the SAR echo signal at the imaging time. The red curve in Fig. 9 represents the estim-

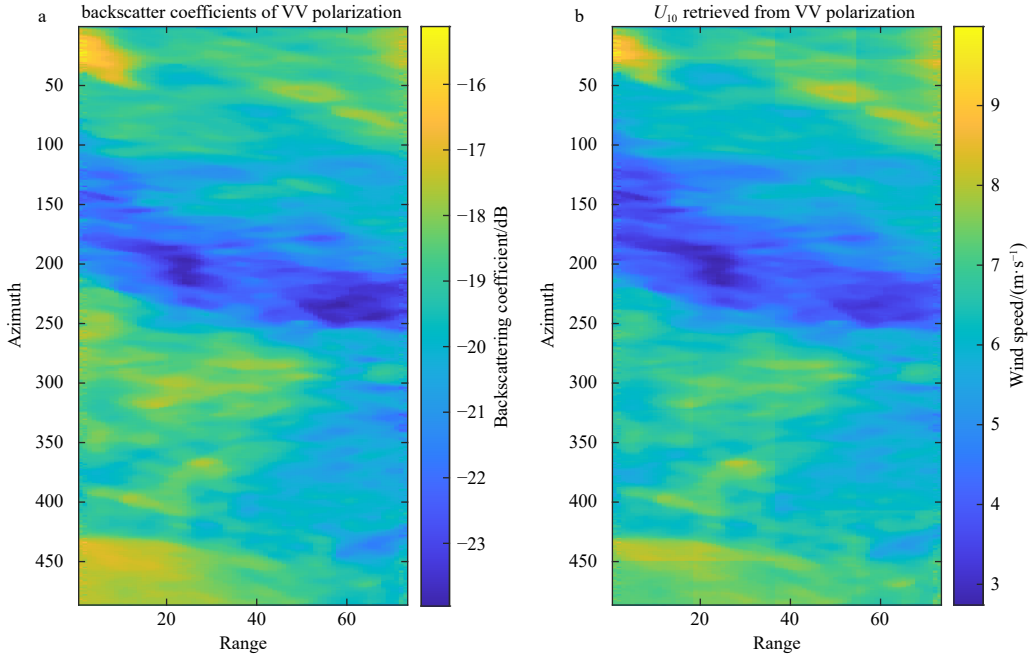

Fig. 10. The backscattering coefficient of VV polarization (a); the sea surface wind retrieved from VV polarization (b). The numerical values of abscissa and ordinate represent the number of points in the range and azimuth of the SAR image after multi-look processing, respectively.

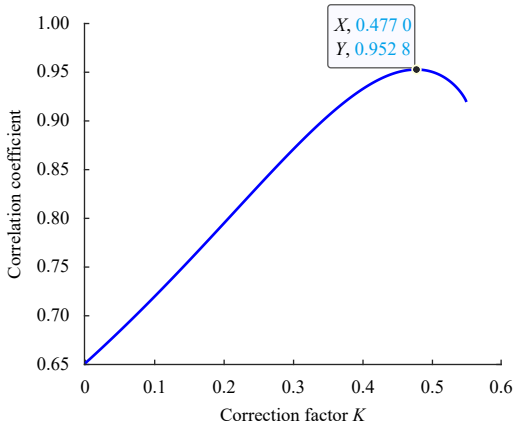

Fig. 11. The correlation coefficient between the VH polarization backscattering coefficient after subtracting the NESZ corrected by the factor K and the wind speed.

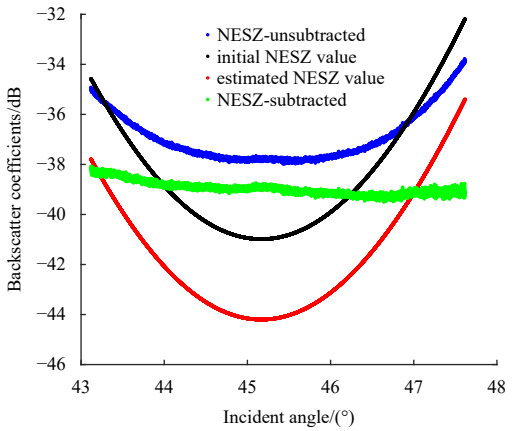

Fig. 12. The backscattering coefficient of VH polarization before and after NESZ subtraction and the change of NESZ before and after error correction with incident angle.

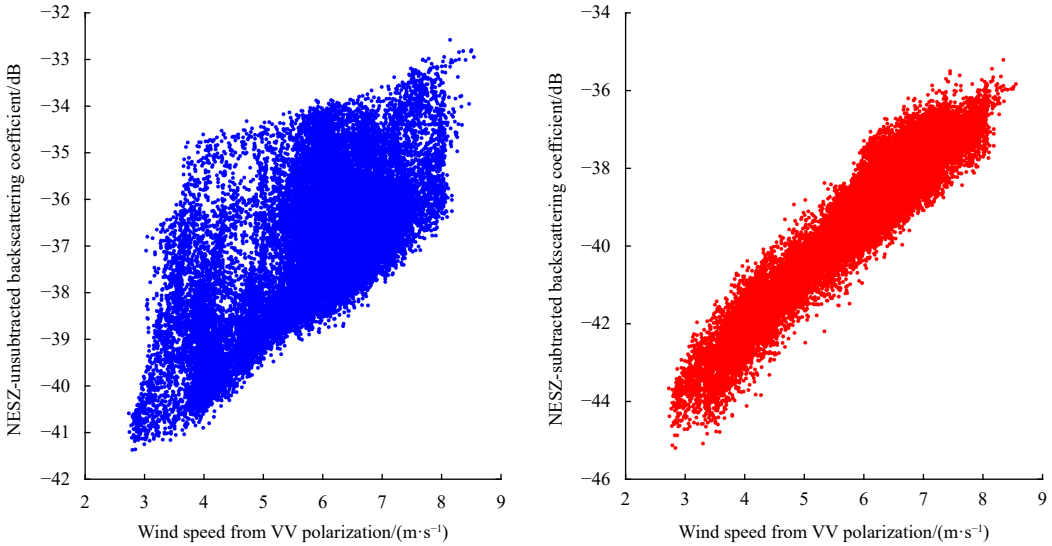

Fig. 13. The scatter diagram of the change of VH polarization backscattering coefficients with wind speed. The blue dot on the left shows the NESZ-unsubtracted backscattering coefficients, and the red dot on the right shows the NESZ-subtracted backscattering coefficients.

Table 5. The correction factors K of this GF3-02 TOPSAR image

Subswath	S1	S2	S3	S4	S5
K(linear)	0.788	0.407	0.594	0.494	0.477
K/dB	–1.032	–3.907	–2.266	–3.065	–3.215

ated NESZ value of the scene image, and the green curve represents the NESZ-subtracted backscattering coefficients. The maximum NESZ value of this image is –33.69 dB, which reflects that the GF3-02 TOPSAR imaging mode has a very low NESZ level.

3.3 *NESZ statistical relationship of GF3-02 TOPSAR*

We performed NESZ estimation on all the data in Table 2. According to the method described in this paper. Figure 14 shows the change of NESZ of the six sub-swaths with the incident angle, where different colored curves represent NESZ in different scenes. The shape of NESZ curves between the same beams is basically the same, and there are only slight differences caused by different slant ranges, which can be ignored. It can be seen that there is only a constant power difference between them. Therefore, we statistically evaluated the minimum values and maximum values of NESZ curves for each group of the beam. The mean values and standard deviation (STD) are shown in Table 6. Therefore, it can be considered that the GF3-02 TOPSAR imaging mode has a good NESZ level and is stable. Of course, with the accumulation of GF3-02 TOPSAR data, there will be further supplementary optimization. Therefore, GF3-02 SAR is very suitable for quantitative retrieval of sea surface environmental parameters under the condition of weak scattering.

Furthermore, the NESZ of GF3-02 TOPSAR mode in the azimuth is shown in Fig. 15, which shows the noise gain normalized curve with azimuth scanning angle in the range of –1.9° to 1.9°. When GF3-02 SAR works at the maximum scanning angle, the noise power has a difference of 4.149 dB between the scanning center and the scanning edge. Therefore, it is necessary to subtract the azimuthal noise under the condition of low SNR. The azimuth scanning gain of noise in dB unit can be calculated as

$$G_{\mathrm{az}}(\phi) = 1.067\,550\,811\,941\,799\phi^2 + 0.15\phi - 0.012\,34. \quad (18)$$

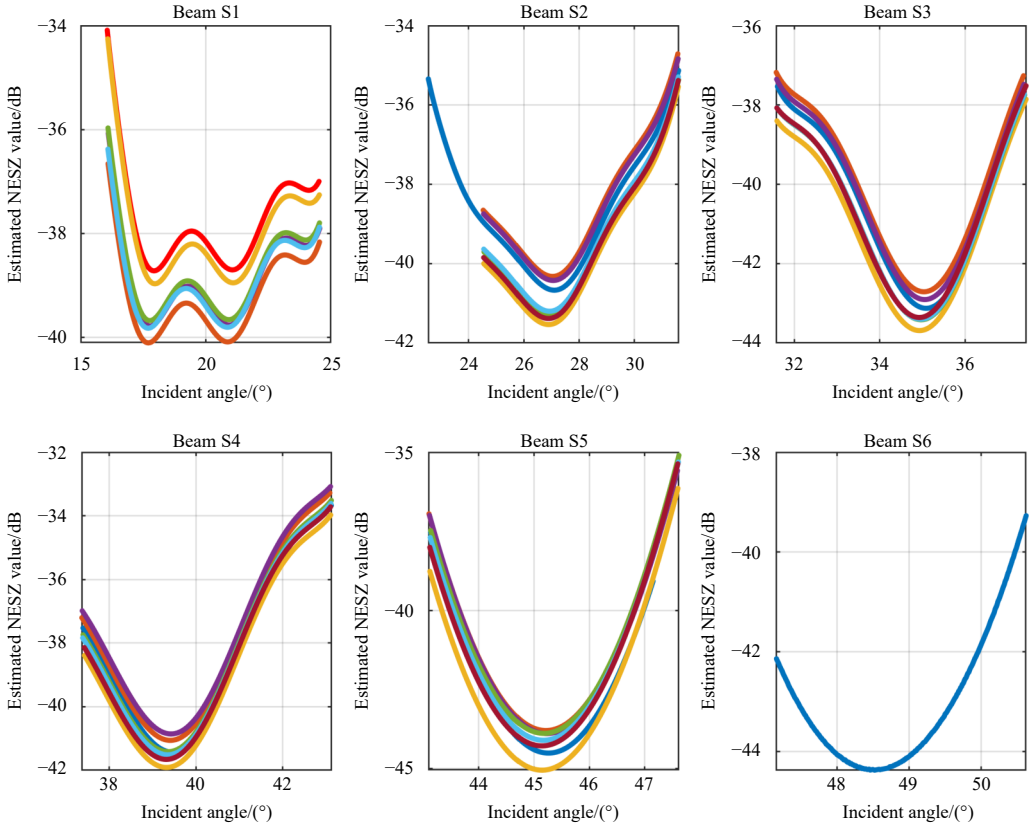

Fig. 14. The estimated NESZ value in the range of GF3-02 TOPSAR data selected in this paper, where different colored curves represent NESZ in different scenes.

Table 6. The mean values and STD of the minimum value and maximum value of NESZ curves for each group of beams

Beam code	Minimum		Maximum	
	Mean/dB	STD/dB	Mean/dB	STD/dB
S1	−39.52	0.54	−35.57	1.11
S2	−40.98	0.49	−35.18	0.31
S3	−43.23	0.34	−37.56	0.24
S4	−41.41	0.36	−33.54	0.29
S5	−44.22	0.46	−35.78	0.84
S6	−44.38	–	−39.27	–

Note: – represents no data.

In addition, here we provide NESZ normalized reference fitting curve of GF3-02 TOPSAR in the range, which can be obtained by high-order polynomial fitting. Specifically, it can be expressed in dB unit as:

$$P_{N_{\text{ref}}}(i) = P_{N_{\text{norm}}}(i) + P_{\text{min}}(i), i = 1, 2, 3, 4, 5, 6, \tag{19}$$

$$P_{N_{\text{norm}}} = [a_1, a_2, a_3, a_4, a_5, a_6, a_7, a_8, a_9, a_{10}, a_{11}, a_{12}] \times \left[\theta^{11}, \theta^{10}, \theta^9, \theta^8, \theta^7, \theta^6, \theta^5, \theta^4, \theta^3, \theta^2, \theta^1, \theta^0\right]^{\text{T}}, \tag{20}$$

where $P_{N_{\text{norm}}}$ is the normalized NESZ curve of GF3-02 TOPSAR in the range, a_i is the polynomial coefficient (see Table 7 for details) and θ is the radar incidence angle, which can be obtained in the incident angle file. P_{min} is the minimum value of the NESZ curve, which can be calculated according to the mean value in Table 6 or the error correction method of NESZ proposed in this paper.

4 Discussion

This paper presents an estimation method of NESZ of the

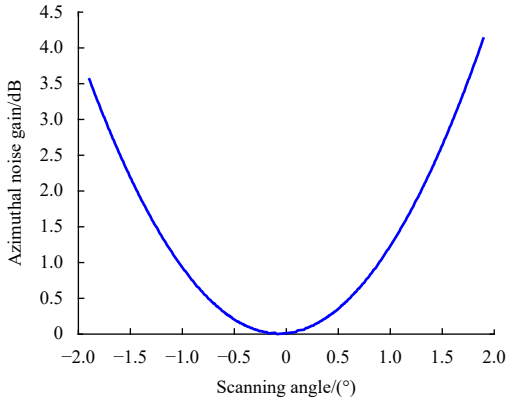

Fig. 15. The normalized NESZ curve of GF3-02 TOPSAR with scanning angle in the azimuth.

GF3-02 TOPSAR imaging mode, which calculates the initial value of NESZ based on the inner calibration noise data of GF3-02 SAR raw data and the noise gain of the imaging algorithm. The NESZ is obtained by theoretical calculation, which can effectively eliminate the dependence of other methods on SAR imaging mode and data quality in a timely manner. However, in the case of low SNR, such as cross-polarization sea surface data with low sea conditions, the error of the initial NESZ value needs to be considered. The proposed method combines the linear relationship between the backscattering coefficient of cross-polarization sea surface and sea surface wind speed and the consistent scattering characteristics of overlapping areas between TOPSAR sub-swaths to compensate the error of the initial value of NESZ, and finally obtain the appropriate NESZ estimation value.

Table 7. The polynomial coefficients of normalized NESZ curve of GF3-02 TOPSAR cross-polarization image in range

	S1	S2
a_1	2.934 662 518 964 063 0×10^{-7}	0
a_2	−6.202 187 341 084 324 0×10^{-5}	3.220 491 988 564 891 0×10^{-6}
a_3	5.888 705 964 990 000 0×10^{-3}	−8.833 628 334 577 523 0×10^{-4}
a_4	−3.310 432 945 730 230 0×10^{-1}	1.087 930 918 828 020 0×10^{-1}
a_5	1.221 840 044 906 902 1×10	−7.922 199 246 366 103 0
a_6	−3.100 263 444 448 249 0×10^{2}	3.777 289 576 734 351 0×10^{2}
a_7	5.496 854 327 201 269 0×10^{3}	−1.232 182 485 188 618 0×10^{4}
a_8	−6.770 699 128 100 621 0×10^{4}	2.784 980 544 619 058 0×10^{5}
a_9	5.625 484 256 308 479 0×10^{5}	−4.306 523 280 385 640 0×10^{6}
a_{10}	−2.954 554 666 615 758 0×10^{6}	4.360 296 957 195 159 0×10^{7}
a_{11}	8.548 181 924 972 551 0×10^{6}	−2.610 234 212 888 801 0×10^{8}
a_{12}	−9.517 966 574 495 262 0×10^{6}	7.015 805 105 520 897 0×10^{8}
	S3	S4
a_1	0	0
a_2	0	0
a_3	0	0
a_4	0	0
a_5	0	0
a_6	5.041 368 255 659 000 0×10^{-3}	4.450 613 749 642 000 0×10^{-3}
a_7	−1.065 018 460 620 902 0	−1.058 418 293 883 211 0
a_8	9.360 503 309 040 074 0×10	1.047 427 756 649 153 0×10^{2}
a_9	−4.381 080 201 949 450 0×10^{3}	−5.521 146 136 503 650 0×10^{3}
a_{10}	1.151 665 299 452 193 0×10^{5}	1.634 924 301 283 721 0×10^{5}
a_{11}	−1.612 176 862 912 459 0×10^{6}	−2.578 744 849 687 035 0×10^{6}
a_{12}	9.389 344 404 762 305 0×10^{6}	1.692 607 263 452 420 0×10^{7}
	S5	S6
a_1	0	0
a_2	0	0
a_3	0	0
a_4	0	0
a_5	0	0
a_6	0	0
a_7	0	0
a_8	−1.379 869 009 031 300 0×10^{-2}	0
a_9	2.490 621 893 160 765 0	0
a_{10}	−1.670 035 310 530 234 0×10^{2}	1.202 019 867 952 835 0
a_{11}	4.928 591 666 155 834 0×10^{3}	−1.167 144 695 658 378 0×10^{2}
a_{12}	−5.397 903 379 950 063 0×10^{4}	2.833 176 378 841 912 0×10^{3}

4.1 *Error analysis of NESZ curves*

The error correction method of the initial value of NESZ proposed in this paper may have the following error sources. On the one hand, in the calculation of the correction factor K of the highest sub-swath, the first premise is to ignore the contribution of the incident angle and the relative wind direction to the backscattering coefficient of the cross-polarization sea surface, and their contribution needs to be proved by further research. It also depends on the accuracy of retrieving wind speed from SAR co-polarization data, which mainly depends on the accuracy of backscattering coefficient of the co-polarization sea surface, the accuracy of ERA5 wind data and the accuracy of GMFs. On the other hand, in the calculation of the correction factors of other sub-swaths, the first premise is to ignore other additional radiation errors. In fact, the difference in backscattering coefficient in the overlapping region between adjacent sub-swaths is not the ideal expression of Eq. (16), and there is only the difference in system thermal noise. It depends on the accuracy of GF3-02 TOPSAR radiation correction, including antenna pattern accuracy, azimuth scanning gain curve accuracy and absolute radiation calibration accuracy. Therefore, long-term on-orbit monitoring and timely maintenance is required to improve the absolute radiation accuracy as a guarantee of the accuracy of NESZ estimation.

4.2 *Relationship between cross-polarized NRCS and wind speed*

In the past decade, different GMFs with a linear relationship between sea surface cross-polarization NRCS and wind speed have been proposed through the analysis of different SAR data, such as RADARSAT-2 and GF-3. (Vachon and Wolfe, 2011; Zhang et al., 2012; van Zadelhoff et al., 2014; Ren et al., 2017; Wang et al., 2018). By considering the contribution of non-Bragg scattering in the cross-polarized band, Zhang et al. (2017) proposed the C-3PO mode function which is dependent on the incident angle. Zhang et al. (2019) proposed S-C2PO, in which NRCS is the quadratic polynomial relationship of wind speed by analyzing the Sentinel SAR cross-polarization data.

In this study, in addition to the 7 TOPSAR images used for NESZ estimation, we collected 12 TOPSAR images and 478 QPS Ⅰ images. For these QPS Ⅰ data, we verified the wind field inversion ability of the co-polarization data (Yang et al., 2022). In order to match ERA-5 spatial resolution, we first performed multi-looking processing in the range of 25 km × 25 km for large breadth TOPSAR data. Then, it was matched with ERA-5 wind data spatially and temporally, with 2 783 points of sea surface data matched in total. The relationship between the NESZ-subtracted backscattering coefficient and ERA-5 wind speed is shown in Fig. 16. The wind speed range of this data set is 0–18 m/s. It is obvious that the existing linear GMF model overestimates the backscattering of the sea surface, especially under the condition of low wind speed, compared with the GF3-02 SAR cross-polarization data after subtracting NESZ. The backscattering coefficient of the VH polarization image is not a simple linear relationship with wind speed but a quadratic polynomial fitting relationship like the red line with the square mark in Fig. 16. In order to observe the dependence of NESZ-subtracted backscattering coefficient on incidence angle, we fit the linear curves of backscattering coefficient and wind speed per 5° incident angle, as shown in Fig. 17. The NESZ-subtracted backscattering coefficient decreases with the increase in incident angle, and the influence of incident angle decreases with the increase in wind speed.

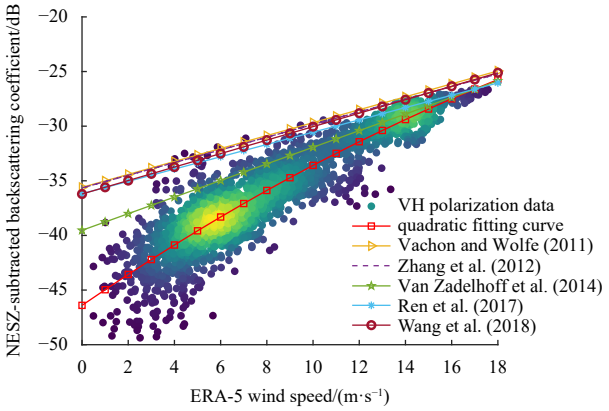

Fig. 16. The relationship between the NESZ-subtracted backscattering coefficient of the VH polarization images collected in this paper and the wind speed of ERA-5, the red line with square markers is the GMF fitted in this paper.

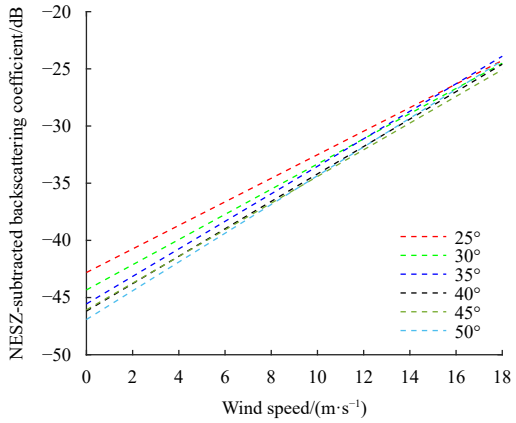

Fig. 17. Linear dependence of NESZ-subtracted backscattering coefficient on wind speeds for incident angle (25°, 30°, 35°, 40°, 45°, and 50°).

In the range of the 25°–50° incidence angle, the NESZ-subtracted backscattering coefficient decreases by 2–4 dB. In addition, we find that the backscattering coefficient does not show obvious dependence on the relative wind direction, so it is not discussed here.

According to Zhang et al. (2017), the following relationship between NESZ-subtracted backscattering coefficient, wind speed and incident angle is obtained:

$$\sigma^0_{\mathrm{VH}} = \left(-0.020\ 05U_{10}^2 + 1.538U_{10} - 46.77\right) \times \left(1 + 0.109\ 5 \times \frac{\theta - 37.5}{37.5}\right), \quad U_{10} < 18\ \mathrm{m/s}, \tag{21}$$

where σ^0_{VH} denotes the NESZ-subtracted backscattering coefficient in unit dB, and 37.5 is the median value of the incident angle. The statistical parameters of bias, root mean square error (RMSE) and correlation coefficient (corr) were used as quantitative indicators of GMF accuracy. The GMF model provided in this paper fits well, with bias of –0.004 8 dB, RMSE of 1.671 dB and corr of 0.939.

Due to the limitations of SAR data, the GMF for GF3-02 SAR needs further verification and correction. Therefore, we will further study the relationship between the sea surface backscattering coefficient of C-band SAR cross-polarization and sea surface wind speed, wind direction and radar parameters by subtracting the GF3-02 TOPSAR cross-polarization data of system thermal noise and the wind speed data provided by reanalysis data, buoy measured data or scatterometer data. On this basis, the error correction of NESZ theoretical calculation values of other imaging modes of GF3-02 SAR, such as strip mode and spotlight mode, can be completed according to this relationship, so as to improve the image quality of GF3-02 SAR. Moreover, we can explore the possibility of using sea SAR data to retrieve SAR range antenna patterns. If this can be achieved, it will eliminate the dependence on the scenes with stable backscatter such as tropical rainforest and realize the monitoring of antenna patterns of various imaging modes of SAR satellites in daily tasks.

5 Conclusions

In this paper, NESZ of GF3-02 TOPSAR image is preliminarily assessed based on inner calibration data and the imaging algorithm, and the estimation process of NESZ is introduced in detail. In particular, an error correction method for the theoretical NESZ curve is proposed based on the relationship between the sea surface backscattering coefficient and the sea surface wind speed, and the same characteristics of the scattering in the overlapping region between adjacent sub-swaths. The effectiveness of the method is verified by the real GF3-02 TOPSAR. The results show that the GF3-02 TOPSAR mode has a shallow noise level, and the overall noise power is less than –33 dB. Even at the center of the beam, the noise power is controlled at about –38 dB. The two-dimensional NESZ reference curve of each beam is provided to GF3-02 TOPSAR users. Users can directly use the reference curve to subtract noise from the TOPSAR image or modify the NESZ curve according to the TOPSAR image with the error correction method of NESZ proposed in this paper or other methods and then conduct accurate quantitative remote sensing research, especially for weak scattering targets. Finally, we provide a preliminary GMF under low wind speed conditions based on the collected GF3-02 SAR cross-polarization data and ERA-5 wind speed data, which depends on the incident angle. Compared with the NESZ-subtracted backscattering coefficient, the bias is –0.004 8 dB, the RMSE is 1.671 dB and the corr is 0.939.

References

Albright W, Nicoll J. 2002. Empirical determination of thermal noise levels in synthetic aperture radar. In: IEEE International Geoscience and Remote Sensing Symposium. Toronto, ON, Canada: IEEE, 2729–2731

Angelliaume S, Dubois-Femandez P, Jones C E, et al. 2018. Oil slick detection in the offshore domain: Evaluation of polarization-dependent SAR parameters. In: IGARSS 2018-2018 IEEE International Geoscience and Remote Sensing Symposium. Valencia, Spain: IEEE, 8096–8099

Curlander J C, McDonough R N. 1991. Synthetic Aperture Radar: Systems and Signal Processing. New York, USA: Wiley

Fan Shengren, Zhang Biao, Mouche A A, et al. 2020. Estimation of wind direction in tropical cyclones using C-band dual-polarization synthetic aperture radar. IEEE Transactions on Geoscience and Remote Sensing, 58(2): 1450–1462, doi: 10.1109/TGRS.2019.2946885

Freeman A. 1992. SAR calibration: An overview. IEEE Transactions on Geoscience and Remote Sensing, 30(6): 1107–1121, doi: 10.1109/36.193786

Freeman A, Curlander J C. 1989. Radiometric correction and calibration of SAR images. Photogrammetric Engineering and Remote Sensing, 55(9): 1295–1301

Hajnsek I, Pottier E, Cloude S R. 2003. Inversion of surface parameters from polarimetric SAR. IEEE Transactions on Geoscience and Remote Sensing, 41(4): 727–744, doi: 10.1109/TGRS.2003.810702

Han Bing, Ding Chibiao, Zhong Lihua, et al. 2018. The GF-3 SAR data processor. Sensors, 18(3): 835, doi: 10.3390/s18030835

Korosov A, Demchev D, Miranda N, et al. 2022. Thermal denoising of cross-polarized Sentinel-1 data in interferometric and extra wide swath modes. IEEE Transactions on Geoscience and Remote Sensing, 60: 5218411

Lu Liao, Yang Jie. 2013. Analysis of the influence of water body on polarimetric SAR calibration. In: IET International Radar Conference 2013. Xi'an, China: IET

Martone M, Bräutigam B, Rizzoli P, et al. 2013. Impact of SAR data quantization on TanDEM-X performance. In: 2013 IEEE International Geoscience and Remote Sensing Symposium. Melbourne, VIC, Australia: IEEE, 4487–4490

Moon W M, Staples G, Kim D J, et al. 2010. Radarsat-2 and coastal applications: Surface wind, waterline, and intertidal flat roughness. Proceedings of the IEEE, 98(5): 800–815, doi: 10.1109/JPROC.2010.2043331

Park J W, Korosov A A, Babiker M, et al. 2018. Efficient thermal noise removal for Sentinel-1 TOPSAR cross-polarization channel.

IEEE Transactions on Geoscience and Remote Sensing, 56(3): 1555–1565, doi: 10.1109/TGRS.2017.2765248

Park J W, Won J S, Korosov A A, et al. 2019. Textural noise correction for Sentinel-1 TOPSAR cross-polarization channel images. IEEE Transactions on Geoscience and Remote Sensing, 57(6): 4040–4049, doi: 10.1109/TGRS.2018.2889381

Ren Lin, Yang Jingsong, Mouche A, et al. 2017. Preliminary analysis of Chinese GF-3 SAR quad-polarization measurements to extract winds in each polarization. Remote Sensing, 9(12): 1215, doi: 10.3390/rs9121215

Scheuchl B, Cumming I. 2005. Analysis of the influence of NESZ variations on cross-polarized signatures of sea ice. In: Proceedings 2005 IEEE International Geoscience and Remote Sensing Symposium. Seoul, Korea(South): IEEE, 5157–5160

Shi Lei, Yang Le, Zhao Lingli, et al. 2021. NESZ estimation and calibration for Gaofen-3 polarimetric products by the minimum noise envelope estimator. IEEE Transactions on Geoscience and Remote Sensing, 59(9): 7517–7534, doi: 10.1109/TGRS.2020.3033534

Torres R, Navas-Traver I, Bibby D, et al. 2017. Sentinel-1 SAR system and mission. In: 2017 IEEE Radar Conference (RadarConf). Seattle, WA, USA: IEEE, 1582–1585

Vachon P W, Wolfe J. 2011. C-band cross-polarization wind speed retrieval. IEEE Geoscience and Remote Sensing Letters, 8(3): 456–459, doi: 10.1109/LGRS.2010.2085417

Valenzuela G R. 1978. Theories for the interaction of electromagnetic and oceanic waves–A review. Boundary-Layer Meteorology, 13(1): 61–85

Van Zadelhoff G J, Stoffelen A, Vachon P W, et al. 2014. Retrieving hurricane wind speeds using cross-polarization C-band measurements. Atmospheric Measurement Techniques, 7(2): 437–449, doi: 10.5194/amt-7-437-2014

Verhoef A, Portabella M, Stoffelen A, et al. 2008. CMOD5. N-the CMOD5 GMF for neutral winds. https://digital.csic.es/bitstream/10261/156198/1/Verhoef_et_al_2008.pdf [2021-12-29/2023-04-03]

Wang Lei, Han Bing, Yuan Xinzhe, et al. 2018. A preliminary analysis of wind retrieval, based on GF-3 wave mode data. Sensors, 18(5): 1604, doi: 10.3390/s18051604

Yang Junxin, Han Bing, Zhong Lihua, et al. 2022. First assessment of GF3–02 SAR ocean wind retrieval. Remote Sensing, 14(8): 1880, doi: 10.3390/rs14081880

Yin Di, Han Bing, Sun Jili, et al. 2021. Calibration method to the impact of antenna scanning on TOPSAR. Journal of University of Chinese Academy of Sciences (in Chinese), 38(6): 791–799

Zhang Qingjun. 2017. System design and key technologies of the GF-3 satellite. Acta Geodaetica et Cartographica Sinica (in Chinese), 46(3): 269–277

Zhang Kangyu, Huang Jingfeng, Mansaray L R, et al. 2019a. Developing a subswath-based wind speed retrieval model for Sentinel-1 VH-Polarized SAR data over the ocean surface. IEEE Transactions on Geoscience and Remote Sensing, 57(3): 1561–1572, doi: 10.1109/TGRS.2018.2867438

Zhang Biao, Mouche A, Lu Yiru, et al. 2019b. A geophysical model function for wind speed retrieval from C-band HH-polarized synthetic aperture radar. IEEE Geoscience and Remote Sensing Letters, 16(10): 1521–1525, doi: 10.1109/LGRS.2019.2905578

Zhang Guosheng, Perrie W, Li Xiaofeng, et al. 2017. A hurricane morphology and sea surface wind vector estimation model based on C-band cross-polarization SAR imagery. IEEE Transactions on Geoscience and Remote Sensing, 55(3): 1743–1751, doi: 10.1109/TGRS.2016.2631663

Zhang Biao, Perrie W, Vachon P W, et al. 2012. Ocean vector winds retrieval from C-band fully polarimetric SAR measurements. IEEE Transactions on Geoscience and Remote Sensing, 50(11): 4252–4261, doi: 10.1109/TGRS.2012.2194157

Zhong Lihua, Qiu Xiaolan, Han Bing, et al. 2019. ScanSAR radiometric correction and analysis of GaoFen-3. In: 2019 6th Asia-Pacific Conference on Synthetic Aperture Radar (APSAR). Xiamen, China: IEEE, 1–4